PHYSICAL REVIEW A **99**, 063625 (2019)

Supersolid phases of Rydberg-excited bosons on a triangular lattice

Jaromir Panas,[1,*] Mathieu Barbier,[1] Andreas Geißler,[1,2] and Walter Hofstetter[1]
[1]*Institut für Theoretische Physik, Goethe-Universität, 60438 Frankfurt am Main, Germany*
[2]*ISIS, University of Strasbourg and CNRS, 67000 Strasbourg, France*

(Received 20 March 2019; published 27 June 2019)

Recent experiments with ultracold Rydberg-excited atoms have shown that long-range interactions can give rise to spatially ordered structures. Observation of crystalline phases in a system with Rydberg atoms loaded into an optical lattice seems also within reach. Here we investigate a bosonic model on a triangular lattice suitable for description of such experiments. Numerical simulations based on bosonic dynamical mean-field theory reveal a rich phase diagram with different supersolid phases. Comparison with the results obtained for a square lattice geometry shows qualitatively similar results in a wide range of parameters; however, on a triangular lattice we do not observe the checkerboard supersolid. Moreover, unlike on a square lattice, we did not find a phase transition from uniform superfluid to supersolid induced by increase of the hopping amplitude on a triangular lattice. Based on our results, we propose an intuitive interpretation of the nature of different supersolid phases. We also propose parameters for the experimental realization.

DOI: 10.1103/PhysRevA.99.063625

I. INTRODUCTION

A supersolid is a phase with simultaneously broken U(1) and translational symmetry of the system. Since the first time it was theoretically discussed [1–4] it has proven difficult to realize in experiment. Supersolids emerging due to long-range interaction between bosonic particles have been experimentally realized with ultracold bosons in optical cavities [5–8]. Other paths to obtain supersolids are intensively studied. A promising experimental approach involves dipolar quantum gases trapped in a harmonic potential or loaded into an optical lattice [9,10]. In the former case, phases with transient supersolid properties have been recently observed [11,12]. The advantage of the approach involving optical lattices is that the resulting system is highly tunable and accurately described by the extended [13,14] version of the Bose-Hubbard model [15,16].

One of the first studies of the extended Bose-Hubbard model in the context of supersolids involved hard-core bosons on a triangular, frustrated lattice with nearest-neighbor interactions [17–20]. In these numerical quantum Monte Carlo (QMC) studies several different phases were observed, including a superfluid, an insulating density-wave, and two supersolid phases. Interestingly, the frustration of the lattice was found to be essential for the formation of the supersolid and for preventing phase separation, which is observed on the square lattice [13].

To obtain a supersolid phase on a square lattice with a hard-core constraint one needs long-range interaction [21,22]. Studies within mean-field [14,23] and QMC [24] have shown that supersolid phases exist in square and cubic lattice models with dipolar interactions between atoms. Long-range interaction also leads to other interesting phenomena, such as the appearance of multiple insulating density-wave phases with commensurate filling in the limit of small hopping amplitude [24–26]. The resulting phase diagram has features similar to the devil's staircase in the Ising model [27–29].

Experimentally, long-range interactions of the van der Waals type can be realized, e.g., by exciting atoms to high principal quantum number Rydberg states [30,31]. The advantage of this approach is that one can tune the strength of the long-range interaction through an appropriate choice of the Rydberg state. Rydberg atoms also have applications in other fields such as quantum information [32], understanding quantum critical behavior [33], and molecule [34,35] and superatom [36,37] formation, among many others [38]. Moreover, loading of Rydberg atoms into an optical lattice and the observation of emerging ordered structures have been achieved experimentally [39–43], although so far only in the frozen limit of a deep lattice potential. In contrast, theoretical studies of the corresponding models have been performed both in the frozen limit and for itinerant atoms. Main results include the study of self-organization of Rydberg excitations in a lattice [29,44,45], phase diagrams and effects of finite hopping amplitude [28,46–48], spectral properties of different phases [49], and effects of dissipation [50–52]. However, these studies focused on the square lattice geometry without considering effects of frustration.

In this work we study a theoretical model appropriate for describing equilibrium phases of atoms coupled to their internal highly excited Rydberg states and loaded into optical lattices. We extend our previous study of a square lattice system [47] by obtaining results for a triangular lattice, frustrated with respect to formation of a checkerboard (super-)solid. We investigate the effect of lattice geometry on the phase diagram. We also study in more detail the properties of the observed supersolid phases, finding that they can be divided into two types.

---

[*] panas@th.physik.uni-frankfurt.de

By assuming thermal equilibrium in our study we neglect many dissipative processes that make experimental realization of supersolids challenging. Nevertheless, better understanding of equilibrium properties of the system might help in overcoming such difficulties. On top of that, following a suggestion from [49] and findings of equilibrium study one can determine parameters suitable for minimizing the destructive effect of avalanche dephasing.

This paper is organized as follows. In Sec. II we introduce the model and briefly discuss our variant of the real-space bosonic dynamical mean-field theory (B-DMFT) method used in the simulations. In Sec. III we present and discuss the results. Section III A is aimed at understanding the effects of the lattice geometry by studying the phase diagrams and properties of observed phases. In Sec. III B we compare the results of B-DMFT and static mean-field theory to estimate the relevance of local quantum fluctuations. In Sec. III C we propose an experimental scheme for minimizing the destructive influence of dissipation induced by coupling to the environment. In Sec. IV our findings are summarized.

II. SYSTEM AND METHOD

A. Model

We choose a model suitable to describe experiments with bosonic alkali atoms, e.g., ^{87}Rb, loaded into a triangular optical lattice [53] and coupled (by an additional laser field) to a Rydberg state with high principal quantum number [39,41]. For each lattice site i we introduce bosonic annihilation operators $\hat{a}_i$ of an atom in its ground state and $\hat{b}_i$ of an atom in its highly excited Rydberg state. The corresponding Hamiltonian reads [46,47]

$$\hat{H} = \hat{H}_{\text{kin}} + \hat{H}_{vdW} + \sum_i (\hat{H}_{\text{loc},i} + \hat{H}_{R,i}). \tag{1}$$

The summation runs over the N lattice sites of the system. In the end we take the thermodynamic limit of $N \to \infty$, assuming the system to be composed of periodically recurring unit cells of finite size N_{uc}.

$\hat{H}_{\text{kin}}$ represents the kinetic energy of atoms tunneling between neighboring lattice sites

$$\hat{H}_{\text{kin}} = -J \sum_{\langle i,j \rangle} (\hat{a}_i^\dagger \hat{a}_j + \eta \hat{b}_i^\dagger \hat{b}_j). \tag{2}$$

Here J is the hopping amplitude, and η represents the ratio between the hopping amplitude of excited-state atoms to that of ground-state atoms. $\langle i, j \rangle$ indicates summation over nearest neighbors i and j. It is useful to introduce the connectivity z of the lattice, which is the number of nearest neighbors for any site. For the triangular lattice $z = 6$.

$\hat{H}_{vdW}$ represents the van der Waals interaction between two excited-state atoms and is given by

$$\hat{H}_{vdW} = \frac{V_{vdW}}{2} \sum_{i \neq j} \frac{\hat{n}_{e,i} \hat{n}_{e,j}}{|\mathbf{i} - \mathbf{j}|^6}, \tag{3}$$

where $|\mathbf{i} - \mathbf{j}|$ is the Euclidean distance between lattice sites i and j divided by lattice spacing a, $\hat{n}_{e,i} = \hat{b}_i^\dagger \hat{b}_i$ is the number operator at site i for the excited bosons, and V_{vdW} is the van der Waals interaction strength, which is given by $V_{vdW} = C_6/a^6$, with C_6 being van der Waals coefficient [31].

$\hat{H}_{\text{loc},i}$ is a local part of the Hamiltonian (for site i) describing the chemical potential and the onsite interaction. It is given by

$$\begin{aligned} \hat{H}_{\text{loc},i} = {} & \frac{U}{2} (\hat{a}_i^\dagger \hat{a}_i^\dagger \hat{a}_i \hat{a}_i + 2\lambda \hat{a}_i^\dagger \hat{b}_i^\dagger \hat{b}_i \hat{a}_i + \tilde{\lambda} \hat{b}_i^\dagger \hat{b}_i^\dagger \hat{b}_i \hat{b}_i) \\ & - \mu (\hat{n}_{g,i} + \hat{n}_{e,i}), \end{aligned} \tag{4}$$

with $\hat{n}_{g,i} = \hat{a}_i^\dagger \hat{a}_i$. The parameters U, λU, and $\tilde{\lambda} U$ describe the local interaction strength between two ground-state atoms, ground-state atom and excited-state atom, and two excited-state atoms, respectively. μ is the chemical potential of an external thermal reservoir, since we work in the grand-canonical ensemble.

The last term in the Hamiltonian, the Rabi term $\hat{H}_{R,i}$, describes coupling between ground- and excited-state atoms, induced by the driving with an additional laser field. Within the rotating wave approximation (RWA), this contribution to the Hamiltonian is given by

$$\hat{H}_{R,i} = \frac{\Omega}{2} (\hat{b}_i^\dagger \hat{a}_i + \hat{a}_i^\dagger \hat{b}_i) - \Delta \hat{n}_{e,i}. \tag{5}$$

Here Ω is the Rabi frequency, and Δ the detuning of laser frequency from that of the atomic transition which we consider.

In the following we set $\hbar = k_B = 1$ and use the Rabi frequency Ω as the unit of energy, unless stated otherwise. We assume the system is in thermal equilibrium at zero temperature.

In our model we set $\lambda, \tilde{\lambda} \gg 1$, leading to a hard-core constraint for excited-state atoms [47]. Rydberg atoms are susceptible to formation of molecules [54] which are not trapped by the lattice potential and therefore lead to a high two-body loss rate. This in turn leads to a hard-core constraint due to the quantum Zeno effect [55–57].

We also set the value of $\eta = 0$, which translates to immobile Rydberg atoms. The effect of nonvanishing η was considered in [47], and only small changes in the values of observables were observed. This is not surprising, as the excited atoms interact strongly via the van der Waals interaction, which leads either to a very small fraction of excited atoms or to crystalline order where kinetic processes are suppressed.

B. Method

We perform calculations with two methods: (i) a Gutzwiller (static) mean-field approximation, described in detail in [16,52], and (ii) the bosonic dynamical mean-field theory (B-DMFT) [58]. Both methods are based on self-consistency and on mapping of the lattice problem onto a set of local impurity problems. In order to be able to do the latter, we treat the nonlocal interaction term within the Hartree approximation [59],

$$\begin{aligned} \hat{H}_{vdW} &= \frac{V_{vdW}}{2} \sum_{i \neq j} \frac{\hat{n}_{e,i} \hat{n}_{e,j}}{|\mathbf{i} - \mathbf{j}|^6} \\ &\approx V_{vdW} \sum_{i \neq j} \left(\hat{n}_{e,i} - \frac{\langle \hat{n}_{e,i} \rangle}{2} \right) \frac{\langle \hat{n}_{e,j} \rangle}{|\mathbf{i} - \mathbf{j}|^6}. \end{aligned} \tag{6}$$

Moreover, both methods are implemented within a real-space approach, which allows us to study arbitrary periodically recurring ordered structures.

Below we will outline the main steps of the B-DMFT approach, referring the reader to [47] for a more detailed discussion. The Gutzwiller mean-field technique may be viewed as a limiting case of B-DMFT and, therefore, it follows similar steps.

1. Frozen limit

To efficiently perform the B-DMFT calculations, we first need to predict what kind of self-organized structures may emerge in the system due to the long-range interaction. We therefore first perform calculations for the frozen gas with $J = 0$. In this limit at unit filling one can map the problem onto an effective spin model [36,41], which, however, is still not trivial to solve on an infinite two-dimensional triangular lattice. We therefore perform another simplification, assuming a negative value of the chemical potential $\mu < 0$, which in the frozen limit leads to a dilute crystal.

Owing to the negative chemical potential and zero temperature, the bosons can reside in the lattice only when their energy is sufficiently lowered by the Rabi term $\hat{H}_R$. When this is the case, the ground state of the system will be a spatially periodic structure with optimal balance between the distribution of bosons in the system and the strength of interaction between them. One can efficiently find Landau free energies of many metastable, spatially periodic states. Each such state is characterized by two spanning vectors $\mathbf{v}_1$ and $\mathbf{v}_2$, see Fig. 1(a). The bosons in the lattice reside only on the sites related by translations defined be these two vectors, forming a sublattice of the underlying triangular lattice. At each occupied lattice site there is exactly one boson $\langle \hat{n}_g + \hat{n}_e \rangle = 1$ in a superposition of a ground and excited state. Comparing the Landau free energies of these metastable ordered states, one can determine the ground state of the system. Structures associated in the frozen limit with a ground state for a certain value of the detuning are considered in the B-DMFT calculation later on.

We note that in the frozen limit a simple expression was found for the critical value of the detuning at which the system undergoes a phase transition to vacuum [47]. This expression can be easily extended beyond the frozen limit, as the transition between the vacuum and a very dilute gas, in which van der Waals–type interactions are negligible, can be treated as a single-particle problem (see also Appendix A). One finds a critical value of the hopping amplitude as a function of the chemical potential, detuning, Rabi frequency, and connectivity:

$$zJ_c = \frac{\Omega^2 + \Delta^2 - (2\mu + \Delta)^2}{4(\mu + \Delta)}. \tag{7}$$

We emphasize that the frozen-limit approach taken here is used primarily to predict most relevant structures for the further B-DMFT and static mean-field calculations. While in the frozen limit we do neglect certain orderings reported for lattice gas models that could not be described with just two Bravais vectors [29,60], we still can recover some of them within B-DMFT (up to certain wavelengths of the structure), because there each site of the unit cell is treated independently. We are not able to describe incommensurate or disordered, e.g., glassy, phases.

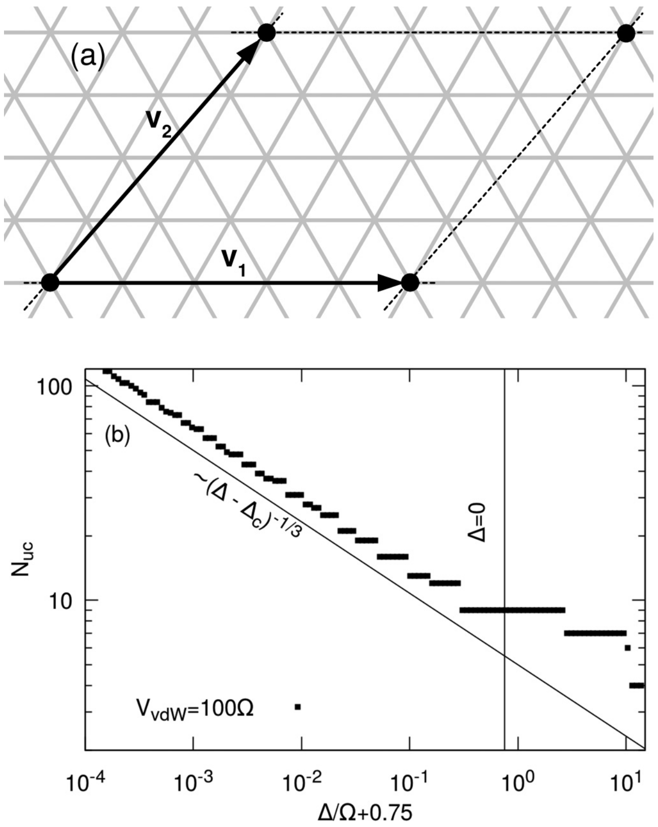

FIG. 1. (a) In the frozen limit occupied sites are related to each other by a translation by linear combinations of $\mathbf{v}_1$ and $\mathbf{v}_2$. (b) In the frozen limit changing the detuning results in a series of phase transitions between different insulating ordered structures characterized by the number of sites per unit cell N_{uc}. Parameters are set to $V_{vdW} = 100$, $U = 0.1$, $\mu = -0.25$, and $J = 0$.

2. B-DMFT

The results of the frozen limit allow us to select the relevant ordered structures and thus to reduce the number of B-DMFT calculations by selecting only those pairs of spanning vectors $(\mathbf{v}_1, \mathbf{v}_2)$ which correspond to some ground state of the system in the frozen limit. Each pair $(\mathbf{v}_1, \mathbf{v}_2)$ defines a unit cell with N_{uc} sites that recurs periodically in the system. Within this unit cell a separate quantum impurity problem corresponds to each site. These impurity problems might have different parameters and solutions, resulting in different values of local observables, such as the condensate order parameter for ground- $\phi_{i,g} = \langle \hat{a}_i \rangle$ and excited-state $\phi_{i,e} = \langle \hat{b}_i \rangle$ bosons, expectation value of the occupation of ground- $\langle \hat{n}_{g,i} \rangle$ and excited-state $\langle \hat{n}_{e,i} \rangle$ bosons, connected local Green functions, self-energies, etc. As for the impurity solver within the B-DMFT calculations, we apply the exact diagonalization method [47,61,62].

Within B-DMFT one needs to define a set of self-consistency equations [58,63]. The first one is given by the local Dyson equation, relating the local interacting connected Green function $\mathbf{G}$, local Weiss field $\mathcal{G}$, and the self-energy $\mathbf{\Sigma}$.

It reads

$$\mathcal{G}_i^{-1}(\mathrm{i}\omega_n) = \mathbf{G}_i^{-1}(\mathrm{i}\omega_n) + \mathbf{\Sigma}_i(\mathrm{i}\omega_n). \tag{8}$$

Note that each object here is a 4×4 matrix, since there are two components due to the Nambu notation for bosonic Green functions [58] and two components due to two types of bosons (ground and excited state) in the lattice.

The second self-consistency equation involves the condensate order parameter and reads

$$\mathbf{\Psi}_i = \left[\mathbf{g}_i^0(0) - \mathcal{G}_i(0)\right]\mathbf{\Phi}_i + \sum_{j:\langle i,j\rangle} J\mathbf{\Phi}_j, \tag{9}$$

where $\mathbf{g}_i^0$ is the Green function of the noninteracting lattice site i decoupled from the rest of the lattice, $\mathbf{\Psi}_i$ is the vector determining the condensate mean field to which the impurity i is coupled, and $\mathbf{\Phi}_j$ is the vector determining the order parameter at site j (which is calculated in the impurity problem). The summation runs over all j which are nearest neighbors of site i.

In standard B-DMFT, the last self-consistency equation would be given by the lattice Dyson equation [58]. Here, however, due to the complexity of the problem and the large spatial structures considered, we used a simpler one. In our approximate approach we determine the Weiss field according to

$$\mathcal{G}_i(\mathrm{i}\omega_n) = \mathbf{g}_i^0(\mathrm{i}\omega_n) - \sum_{j:\langle i,j\rangle} J^2\mathbf{G}_j(\mathrm{i}\omega_n). \tag{10}$$

Such a self-consistency equation would become exact in the limit of the infinite connectivity Bethe tree [58]. In a finite spatial dimension it amounts to neglecting: (i) the effect which removing a site from the lattice has on the lattice Green functions, and (ii) correlations between different neighbors of the impurity. A similar (though not identical) self-consistency equation has been successfully used for lattices in finite dimensions in the context of real-time dynamics [64]. In Appendix B we elaborate on the effect of this approximation.

Having obtained the self-consistent solution, one can use the local quantities calculated in the impurity problems to determine values of nonlocal quantities. Most importantly, one can calculate the Landau free energy [47]. Note that we have included the chemical potential into the Hamiltonian (1) and are working at zero temperature; therefore the Landau free energy per lattice site is given by $f = \langle \hat{H} \rangle / N$.

3. Obtaining the phase diagram

In order to obtain the phase diagram of the system with respect to the hopping amplitude J and detuning Δ we proceed according to the following steps. First we set the values of the parameters that remain constant throughout the calculations, including V_{vdW}, U, μ, and Ω. Next, within the range of variability of Δ we perform frozen-limit calculations ($J = 0$) and thus obtain a set of unit cells that correspond to the ground state of the system for certain Δ, i.e., unit cells listed in Table I. Once this has been done, one can proceed to the actual B-DMFT calculations. To cover the entire phase diagram, we perform a sweep over different values of J and Δ. Below we describe the steps taken for each pair of values (J, Δ).

TABLE I. Spanning vectors $\mathbf{v}_1$ and $\mathbf{v}_2$ and number of sites in the unit cell N_{uc} of the structures considered in the B-DMFT calculations (except for the first one with $N_{uc} = 3$, which was not considered explicitly but rather implicitly as a special case of the one with $N_{uc} = 9$). $\mathbf{v}_1$ and $\mathbf{v}_2$ are given in the basis of primitive vectors of a triangular lattice $\mathbf{e}_1$ and $\mathbf{e}_2$, e.g., $(3, -1)_\mathbf{e} = 3\mathbf{e}_1 - \mathbf{e}_2$. The primitive vectors in Euclidean space in units of the lattice spacing a are $\mathbf{e}_1 = (1, 0)$ and $\mathbf{e}_2 = (\frac{1}{2}, \frac{\sqrt{3}}{2})$.

$\mathbf{v}_1$	$(2, -1)_\mathbf{e}$	$(2, 0)_\mathbf{e}$	$(3, -1)_\mathbf{e}$	$(3, -1)_\mathbf{e}$
$\mathbf{v}_2$	$(1, 1)_\mathbf{e}$	$(0, 2)_\mathbf{e}$	$(0, 2)_\mathbf{e}$	$(1, 2)_\mathbf{e}$
N_{uc}	3	4	6	7
$\mathbf{v}_1$	$(3, 0)_\mathbf{e}$	$(4, -2)_\mathbf{e}$	$(4, -1)_\mathbf{e}$	$(4, 0)_\mathbf{e}$
$\mathbf{v}_2$	$(0, 3)_\mathbf{e}$	$(2, 2)_\mathbf{e}$	$(1, 3)_\mathbf{e}$	$(0, 4)_\mathbf{e}$
N_{uc}	9	12	13	16

For a given pair (J, Δ) we perform a separate B-DMFT calculation for each of the unit cells listed in Table I. These are initialized in such a way as to break the translational symmetry according to the shape of the unit cell. The U(1) symmetry is also randomly broken to allow for supersolid and superfluid solutions. Next, each self-consistency calculation is performed independently converging onto some metastable state with a finite or vanishing condensate order parameter $\langle \hat{a}_i \rangle$. On top of that, for a given unit cell each converged solution can have: (i) the same spatial structure as the one with which it was initialized, with slightly different values of the local observables, (ii) different, but still nontrivial spatial structure, and (iii) vanishing spatial ordering resulting in a homogeneous phase. From each B-DMFT calculation we also obtain the Landau free energy of a given metastable solution. We identify the solution with the lowest value of the Landau free energy as the ground state for given J and Δ.

III. RESULTS

In this section we present the results of our calculations. In Sec. III A we set the system parameters to be comparable to those used in [47], where the same model on a square lattice has been studied with B-DMFT. This allows us to investigate how the triangular lattice geometry affects the behavior of the system. We also study the nature of different phases observed. In Sec. III B we compare the static mean-field and the B-DMFT results to estimate the significance of local quantum fluctuations. These two sections are aimed at giving a better understanding of phases emerging due to the competition of long-range interaction and kinetic processes on a triangular lattice. In Sec. III C we study a system with experimentally more feasible parameters. We investigate the possibility of observing supersolid phases in a triangular optical lattice with Rydberg atoms. To minimize dissipative effects, we follow the idea suggested in [49] of using an inhomogeneous profile of the Rabi laser.

A. Phase diagram

We choose the following parameters of our system: $V_{vdW} = 100\ \Omega$, $U = 0.1\ \Omega$, and $\mu = -0.25\ \Omega$. As discussed earlier, we also set $\lambda = \tilde{\lambda} = 10^6 \gg 1$ and $\eta = 0$. These parameters

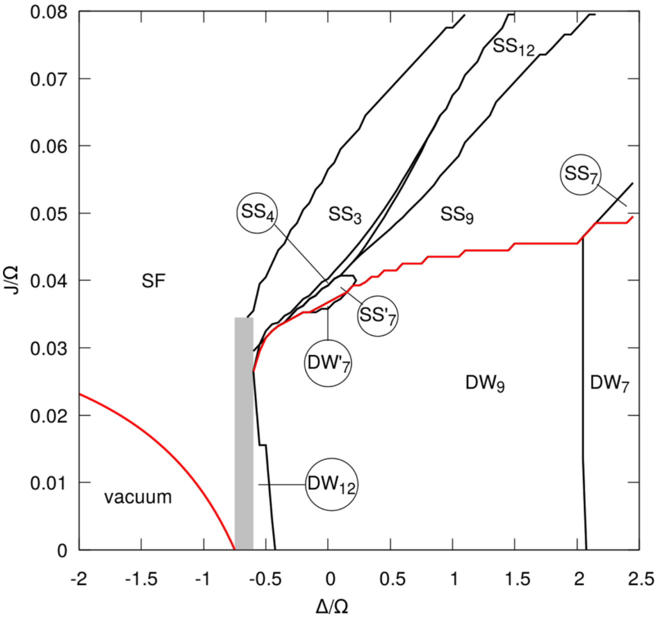

FIG. 2. Phase diagram of the system described by the Hamiltonian (1) obtained from B-DMFT calculations. Parameters of the system are the same as in Fig. 1, except for the variable hopping amplitude J. Phases shown in Fig. 3 are labeled SS_n and DW_n, where the lower index $n = N_{uc}$ represents the number of sites in a unit cell, cf. Table I. Gray shading represents an area where B-DMFT calculations did not converge. The red line separates phases breaking the U(1) symmetry from those where it is preserved. For $\Delta < -0.75$ we use formula (7), as it accurately matches the B-DMFT data.

are the same as in [47], allowing for comparison of square and triangular lattices. Values of the hopping amplitude and the detuning are varied.

We first investigate the frozen-limit case $J = 0$. In Fig. 1(b) we show how the size of the unit cell of the ground state, given by its number of lattice sites N_{uc}, depends on the detuning. Below a critical value of $\Delta_c = -0.75$ the system is empty. As we increase Δ above Δ_c we observe a series of phase transitions between insulating ordered (density-wave) phases, resembling the devil's staircase observed in the Ising model [27–29]. Each has a different translational symmetry and size of the unit cell. For values of Δ close to Δ_c the unit cell is large, resulting in a very dilute system. As the value of the detuning is increased, the density of bosons also increases. These results are qualitatively similar to the ones obtained for a square lattice [47]. The trend line close to Δ_c follows $N_{uc} \sim (\Delta - \Delta_c)^{-\frac{1}{3}}$. The exponent is determined by the spatial dimensionality of the system divided by the exponent in the interaction potential, cf. Appendix A.

Next we proceed to the discussion of the finite hopping $J > 0$ case within the B-DMFT calculations. Out of a large set of unit cells considered in the frozen limit we have selected only the few smallest, relevant for the vicinity of $\Delta = 0$, due to the computational complexity of B-DMFT calculations. They are listed in Table I. According to the frozen-limit results, the structures that were left out become relevant only in the narrow region of detuning, $-0.75 < \Delta < -0.7$. For other values of Δ the structures from Table I should be sufficient.

The phase diagram obtained within B-DMFT is shown in Fig. 2, while the density-wave patterns observed in different phases are shown in Fig. 3. The phases labeled as DW_7, DW_7', DW_9 and DW_{12} are insulating while SS_3, SS_4, SS_7, SS_7', SS_9, SS_{12} are supersolid. A lower index indicates the number of sites in the unit cell N_{uc} of the structure, cf. Table I. In the limit of small hopping amplitude $J = 0.001$ we recover the results of the frozen limit, as expected. The observed structures DW_7 and DW_9 (and DW_{12}, not shown in Fig. 3) follow the trend presented in Fig. 1. Only the sites of a sublattice defined by vectors $\mathbf{v}_1$ and $\mathbf{v}_2$ are occupied. On each of its sites there is a single boson, which is in a superposition between the ground and excited state. The remaining sites of the lattice are nearly empty.

Next we consider the effect of increasing hopping amplitude. For $\Delta < \Delta_c = -0.75$, increasing J leads to a phase transition from the vacuum to a homogeneous superfluid phase. The phase boundary obtained with B-DMFT agrees well with the expression (7). We note that below Δ_c, unlike for the square lattice geometry, where a checkerboard supersolid was found [47], the triangular system does not exhibit any supersolid phase. For $\Delta > -0.6$ small values of the hopping amplitude have only a minor influence on the insulating phases, resulting in small shifts of the phase boundaries with increasing J. Further increase of J eventually leads to a spontaneous breaking of the $U(1)$ symmetry in the system and a transition into one of many supersolid phases.

We observe that at higher values of Δ the supersolid phases immediately above their insulating counterparts have similar order, cf. Fig. 3, $\text{DW}_7 - \text{SS}_7$ and $\text{DW}_9 - \text{SS}_9$. In these phases, namely, SS_7 and SS_9, a significant (when compared to ground-state population) number of excited-state bosons is present. We observe that both the local ground-state condensate order parameter $\langle \hat{a}_i \rangle$ as well as local fluctuations of the occupation $\delta n_i^2 = \langle (\hat{n}_{g,i} + \hat{n}_{e,i})^2 \rangle - \langle \hat{n}_{g,i} + \hat{n}_{e,i} \rangle^2$ (see Appendix B) are much smaller on the sites with excited-state bosons than on the surrounding sites with small excited-state occupation [65]. We interpret this phase as a supersolid which consists of (i) frozen bosons being in a superposition of ground and excited states (with significant fraction of both) residing in the periodic sublattice of the original lattice, and (ii) delocalized condensed bosons, predominantly of the ground-state nature, flowing without friction in the remaining lattice sites. This interpretation is also consistent with the shape of the supersolid–density-wave phase boundary for larger detunings. For a given ordered structure the delocalized bosons can slightly reduce their energy by a small admixture of the excited state, thus increasing the supersolid regime in the phase diagram. This energy reduction is however diminished with increasing fraction of excited-state bosons in the "frozen" sites due to strong nonlocal interaction forces. Hence with increasing Δ the phase boundary is shifted to higher values of J as the fraction of excited bosons on the "frozen" sites increases.

The supersolid phase SS_{12} appears to be of the same nature as SS_7 and SS_9 but with a different spatial structure. The DW_{12} phase (not depicted in Fig. 3), a U(1) symmetric counterpart of the SS_{12} phase, appears for small J around $\Delta \approx -0.5$, cf. Fig. 2. However, SS_{12} and its insulating counterpart are not immediately connected in the phase diagram due to the emergence of other phases discussed further in the text.

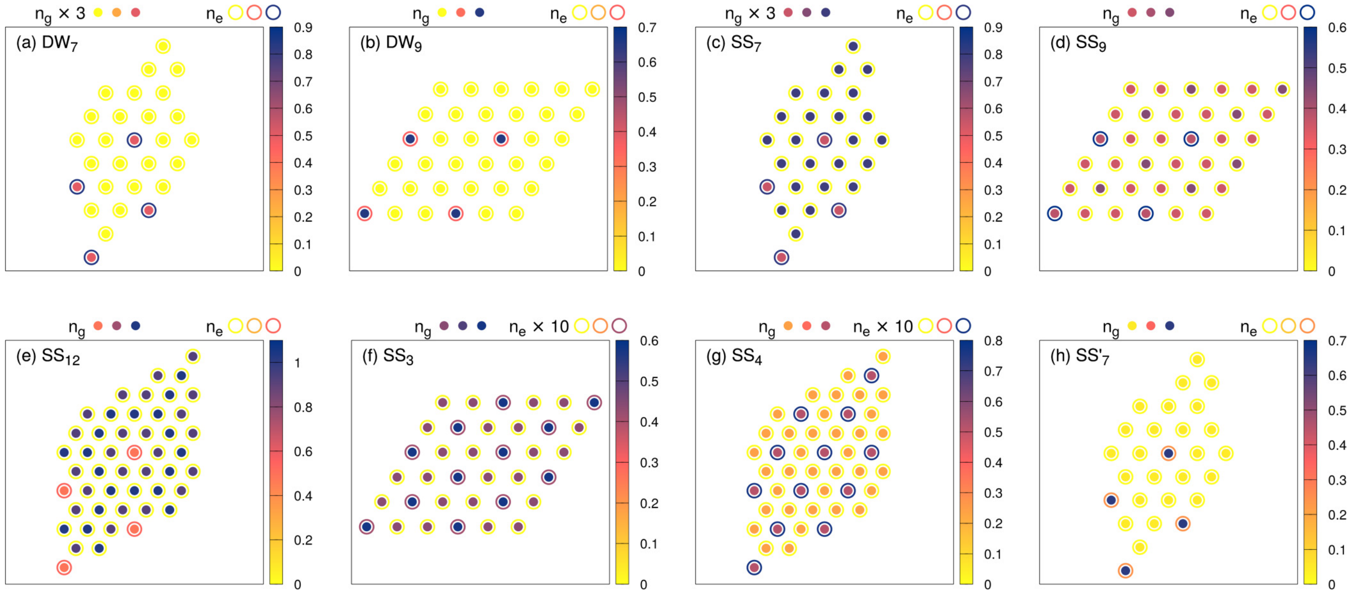

FIG. 3. Structures of selected phases observed in Fig. 2 at (a) $\Delta = 2.45,\ J = 0.001$; (b) $\Delta = 0,\ J = 0.001$; (c) $\Delta = 2.45,\ J = 0.053$; (d) $\Delta = 1,\ J = 0.05$; (e) $\Delta = 1,\ J = 0.06$; (f) $\Delta = 0,\ J = 0.045$; (g) $\Delta = 0,\ J = 0.04$; and (h) $\Delta = 0,\ J = 0.038$. Color represents the fraction of ground- (filled circles) and excited-state (empty circles) bosons per lattice site. Each graph represents sites within a quadrupled unit cell of an initial guess. Each site in a unit cell defines a different impurity problem in the B-DMFT procedure. The depicted patterns recur periodically in the lattice. The fractions of excited- (ground-) state bosons have been rescaled in certain cases for better visibility.

Starting from the SS_9 or SS_{12} phases and decreasing the detuning Δ or increasing the hopping amplitude J, we observe further phase transitions, cf. Fig. 2. Qualitatively different supersolids emerge, labeled as SS_3 and SS_4. These are characterized by the following features. The fraction of the excited-state bosons is significantly (by approximately an order of magnitude) lower than in SS_7, SS_9, or SS_{12}. The wavelength of the density-wave pattern is significantly smaller, with smaller distances between sites with nonvanishing fraction of excited-state bosons. On these sites we have also observed an increase in condensate fraction and local fluctuations of the occupation, cf. Appendix B. Finally, we observe a larger density of atoms in the remaining, intermediate sites and more uniform distribution of the condensate order parameter. This behavior with decreasing values of Δ is opposite of what one would expect if here one tried to apply intuition gained from the frozen limit. Because of these differences, we conclude that this must be a qualitatively different type of supersolid where we can no longer apply the interpretation of "frozen" sublattice sites occupied by the excited-state bosons coexisting with condensed ground-state bosons in between. These phases bear some resemblance to bubble supersolids [66–69] in that the condensation originates from the sites with nonvanishing excited-state fraction, in contrast to the SS_7, SS_9, and SS_{12} phases. We also suspect that the supersolids observed in SS_3 and SS_4 could be connected with the concept of defectons [2,67], which is a condensation of defects (holes) in the ordered structure that are tunneling between different sites. This interpretation seems to be consistent with the observed features of the phases: (i) larger local fluctuations on the sublattice could be related to the presence and condensation of defectons, (ii) a smaller wavelength of the observed pattern supports tunneling of defectons in opposition to the larger wavelength patterns, which are more favorable for the condensation of the ground-state bosons on the intermediate sites (between the site of the sublattice). However, these arguments alone are not sufficient to confirm this interpretation unambiguously.

It is worth mentioning that there is a relation between the SS_9 and SS_3 phases, as well as between SS_{12} and SS_4 phases. In both cases the symmetry of the former phase can be viewed as a reduced version of the symmetry of the latter phase with N_{uc} reduced by a factor of 3, cf. Fig. 3. However, the SS_{12} and SS_4 phases, between which we observed a first-order phase transition, separate the SS_9 and SS_3 phases from each other.

Regarding the two types of supersolids described above, we note that similar observations were made in [48]. There, also, two types were found, with one consisting of a supersolid of bare (ground-state) species and a crystalline phase of dressed (coupled to excited-state) species. However, due to a different model, the second type of supersolid in [48] is not of the same nature as observed here—one does not observe a significant reduction of the wavelength of the periodic structure but rather an increase.

We also observe a phase at intermediate values of the hopping amplitude $J \approx 0.038$ and in the vicinity of detuning $\Delta = 0$ which is depicted in Fig. 3 and labeled SS'_7. It has similar properties to the SS_3 and SS_4 phases, which have a smaller wavelength than the phases at larger detuning, e.g., SS_9, and for which condensation originates from the sites with nonvanishing excited-state fraction, cf. Appendix B. The distinguishing features of SS'_7 are that the fraction of excited-state bosons is significantly higher than in SS_3 or SS_4, and that we also observed an insulating counterpart of the SS'_7 phase, namely, the DW'_7 phase. Both do not occur in the mean-field calculations, as discussed in the next section.

We note that the results presented here are qualitatively similar to those presented in [47] for a square lattice. A

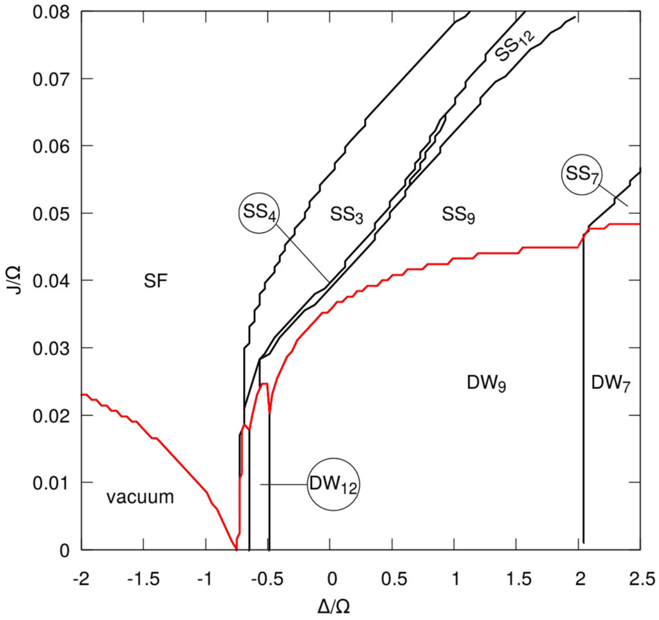

FIG. 4. Phase diagram obtained within the Gutzwiller (static) mean-field approach. The parameters are the same as in Fig. 2.

significant difference is visible here only near the boundary between superfluid and supersolid phases. On a square lattice this boundary separates the superfluid from a checkerboard supersolid, which extends to values of detuning below Δ_c, where one can induce a phase transition from superfluid to supersolid by increasing (rather than decreasing) the hopping amplitude. On a triangular lattice the checkerboard supersolid cannot exist due to frustration, and no supersolid phase exists below Δ_c. Apart from this the two phase diagrams are similar. We attribute this to the fact that the spacing (wavelength) in the majority of structures observed here is larger than the lattice spacing. In this case the difference in geometry of the two lattices has a weaker impact. For these longer-wavelength structures it is actually the square lattice that becomes more frustrated with respect to the favored (due to van der Waals interaction) Wigner crystal formation [29] than the triangular lattice.

B. Comparison with the static mean field

In Fig. 4 we present the results of calculations performed within the static Gutzwiller mean-field approximation [16,52]. Upon comparison with the B-DMFT, we notice that both methods give similar results. The main features of the phase diagrams agree well. Below we focus on the most relevant differences.

As the static mean-field approach favors ordered phases, we expect a phase transition between insulating and superfluid (supersolid) phases to appear at lower values of the hopping amplitude. Indeed, comparing Fig. 2 with Fig. 4 we observe that the boundary of the insulating phases is shifted downwards. This effect is almost negligible for larger absolute values of the detuning and becomes relevant only in the region $|\Delta| \lessapprox 0.75$. This is also a region where an increasing number of phases compete in the system. It seems that only in this region will local quantum fluctuations significantly affect the system's behavior.

Another discrepancy arises from the oversimplification of the insulating phases within the static mean-field approach. The boundaries between different phases with $U(1)$ symmetry do not depend on the hopping amplitude, and their positions are uniquely defined by the detuning. In contrast, B-DMFT calculations show that finite hopping can induce a phase transition between two density-wave phases.

The above two observations are directly related to the most significant difference that we observed. Namely, in the static mean field neither the supersolid SS_7' nor the density-wave DW_7' phase was observed, which should be present according to B-DMFT, cf. Fig. 2. This occurs in the region where we observed the largest discrepancies between the two methods in the values of the condensate order parameter and in properties of the insulating density-wave phase. We conclude that as the detuning Δ approaches critical value $\Delta_c = -0.75$ at intermediate values of the hopping amplitude, effects of local quantum fluctuations become significant (this is further backed up by comparing different self-consistency conditions, Appendix B). At this point we emphasize for clarity that nonlocal fluctuations are treated in both methods on the same level (Hartree mean field). Therefore, we cannot make definite statements about their significance.

The last discrepancy between the results of B-DMFT and static mean field can be observed in the extent of the SS_4 and SS_{12} phases. In static mean field it is slightly smaller than in B-DMFT due to larger extent of the SS_9 phase. Nevertheless, the remaining features of the phase diagram are qualitatively accurately captured by the static mean field. As this method is significantly less demanding computationally, it is the best that we can do at this stage to get some insight into the critical region of $\Delta \approx \Delta_c$, where it is difficult to obtain converged B-DMFT results. We study this region of the phase diagram in Fig. 5. As we approach Δ_c from above, we encounter a series of phase transitions forming a devil's staircase (note the logarithmic scale), both of the insulating density-wave phases at small hopping amplitude, as well as of the supersolid phases for larger hopping. When investigating the devil's staircase in the supersolids we notice that increasing the hopping amplitude seems to favor longer-wavelength structures, shifting the devil's staircase pattern to higher detunings. This is similar to what we observed for $\Delta \gtrapprox 1$, cf. Fig. 4. However, this trend seems to be reversed at the intermediate detuning of $\Delta \gtrapprox -0.68$, which coincides with the onset of the SS_3 phase (short wavelength) for larger hopping amplitudes. We suspect that this might be a feature emerging due to the competition between the two general types of supersolid discussed in Sec. III A and could lead to a multicritical point around $\Delta \approx -0.68$ and $J \approx 0.022$. However, investigating this region within a more accurate B-DMFT method requires improvements of our implementation of the method and goes beyond the scope of this work.

C. Finite-size system with inhomogeneous Rabi frequency

In Sec. III A we have established a relation between the behavior of long-range interacting bosons on the triangular and square lattices. In order to make this comparison, we

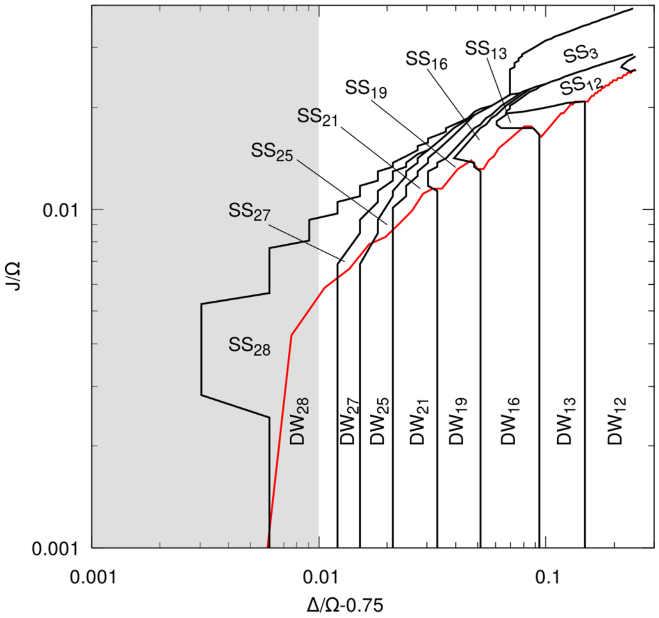

FIG. 5. Phase diagram obtained within the Gutzwiller (static) mean-field approach in the critical region. The parameters are the same as in Fig. 2. Gray shading represents the range of parameters beyond the limit of accuracy of the method due to the maximal size of the considered crystalline structure.

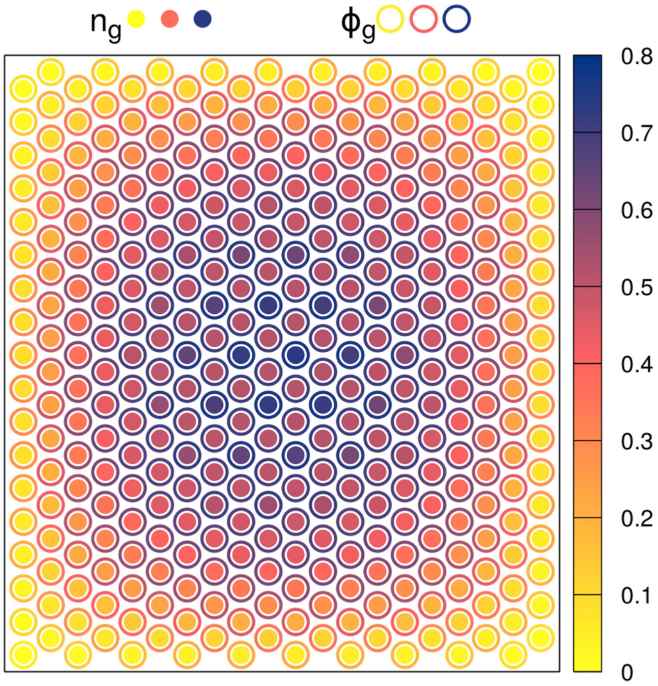

FIG. 6. Ground-state occupation $\langle \hat{n}_{g,i} \rangle$ (filled circles) and condensate order parameter $\phi_{g,i} = \langle \hat{a}_i \rangle$ (empty circles) in real space for an inhomogeneous Rabi frequency Ω_i given by (12). The parameters of the system are $J = 0.0045\ \Omega$, $\mu = -0.025\ \Omega$, $U = 0.01\ \Omega$, $\Delta = -4\ \Omega$, $V_{vdW} = 1.6 \times 10^4\ \Omega$.

have chosen the same parameters as used in [47]. However, these values of the parameters are not optimally suited for experimental realization of the model (1) with Rydberg atoms loaded into an optical lattice. Relatively large values of the hopping amplitude J and small values of the van der Waals interaction V_{vdW} with respect to the Rabi frequency would require using a Rydberg-excited state with low principal quantum number $n \sim 16$. These states have a short lifetime due to spontaneous emission and dephasing processes induced by the blackbody radiation [70]. Below we propose more realistic parameters, which can be chosen based on the observations made in the previous sections and which might help in tackling one of the most notorious experimental challenges—avalanche dephasing [41,49,71].

Avalanche dephasing occurs when a blackbody-radiation-induced transition of a single excited atom to another Rydberg state might trigger a rapid loss of atoms from the system. The average time after which such a process occurs is given by [71]

$$\tau_c = \tau \left(b \sum_i \langle \hat{n}_{e,i} \rangle \right)^{-1}, \tag{11}$$

where b is the branching ratio of the excited state. τ_c is inversely proportional to the total number of excited-state atoms in the system. Therefore, the best candidate for experimental observation of a supersolid phase is the SS_3 phase, where the excited-state fraction is very low. However, since in (11) the total number of Rydberg atoms in the system appears, rather than their density, we need to consider relatively small system sizes. This leads to the further issue of increased Rydberg fraction at sharp edges of the finite-size system, such as shown in [45,49]. In order to avoid this problem, we additionally choose a Gaussian profile of the Rabi laser with a narrow waist on the order of several micrometers, as suggested in [49], given by

$$\Omega_i = \Omega \exp\left[\frac{|\mathbf{i} - \mathbf{0}|^2}{\kappa^2} \right], \tag{12}$$

with $\mathbf{0}$ corresponding to the position of the center of the system and Ω_i an effective Rabi frequency at site i.

Taking the above restrictions into account, we consider a system with bosonic ^{87}Rb atoms loaded into a two-dimensional triangular optical lattice, e.g., such as described in [53] with lattice spacing $a \approx 0.5\ \mu$m. For such a system one should be able to achieve a hopping amplitude of approximately $\sim 0.45\hbar$ kHz [53]. The local interaction is a tunable parameter, which we set to $U = 1\hbar$ kHz. We choose to couple the ground state to an excited $|26S\rangle$ Rydberg state by the Rabi term. Using this $|26S\rangle$ state on a lattice with spacing $a \approx 0.5\ \mu$m gives a van der Waals interaction strength on the order of $V_{vdW} \approx 1600\hbar$ MHz [31] and mean lifetime of $\tau \approx 10\ \mu$s [70]. Rabi frequency and detuning on the order of $\Omega \approx 0.1\hbar$ MHz, $\Delta = -0.4\hbar$ MHz should also be feasible experimentally. The remaining issue is to focus the Rabi laser such that it has a Gaussian profile (12) with $\kappa = 3.5\ \mu$m.

Setting everything in units of Ω and a, we obtain the parameters of the simulation to be the following: $J = 0.0045\ \Omega$, $\mu = -0.025\ \Omega$, $U = 0.01\ \Omega$, $\Delta = -4\ \Omega$, $V_{vdW} = 1.6 \times 10^4\ \Omega$, and $\kappa = 7a$. The resulting density pattern is shown in Fig. 6. In the center of the system we observe the same structure as in the SS_3 phase. Its visibility, defined as

$$\mathcal{V} = \frac{\langle \hat{n}_{g,i} \rangle - \langle \hat{n}_{g,j} \rangle}{\langle \hat{n}_{g,i} \rangle + \langle \hat{n}_{g,j} \rangle}, \tag{13}$$

where i corresponds to the site with maximal occupation and j to the nearest neighbor of i, has the value $\mathcal{V} \approx 0.175$.

Lastly we note that the average total number of atoms in the system is $\sum_i \langle \hat{n}_{g,i} + \hat{n}_{e,i} \rangle \approx 113$ while the average total number of Rydberg excitations is $\sum_i \langle \hat{n}_{e,i} \rangle \approx 0.0373$. Together with the branching ratio on the order of $b \approx 0.1$ [71], the average time after which the avalanche is set off is $\tau_c \approx 3$ ms, which is comparable with the characteristic timescale of the hopping process $t \sim \hbar/J$ and thus is promising for experimental realization.

While the above approach might help in reducing some of the problems that are related to a large fraction of Rydberg atoms in the system, there are still numerous remaining challenges to be dealt with. One still needs to prepare the system so that it is close to its ground state. How to do this while avoiding destructive dissipative effects due to inelastic scattering [54] or dephasing during the state preparation remains an open question. One should also determine whether other dissipative effects will destroy the coherence of the supersolid phase. Some steps to answer this last question have been investigated in [52].

IV. CONCLUSIONS

In this work we have studied the effect of frustration on the formation of crystalline and supersolid states in the extended Bose-Hubbard model with two bosonic species—one itinerant and one subject to two-body van der Waals long-range interaction. The two species are also coupled by a Rabi term and local interaction. We have focused on a system at zero temperature, without including explicitly the effects of coupling to the environment. We have also used the Hartree mean-field approximation to decouple the long-range interaction term.

Within B-DMFT the same model has been previously investigated on a two-dimensional square lattice [47]. Here we solve the problem with two methods: B-DMFT and the Gutzwiller static mean-field approach. Comparison of the B-DMFT results for the two lattice geometries allowed us to determine the effect of the (frustrated) triangular geometry on ordered states. Comparison of B-DMFT results to those of the static mean-field approach allowed us to estimate the significance of local quantum fluctuations.

We have obtained a rich phase diagram, including insulating density-wave, superfluid, and supersolid phases. We observed that the phase diagram on the triangular lattice is qualitatively similar to the one observed for a system with square lattice geometry [47]. Within the parameter regimes considered the only significant discrepancy is the absence of the checkerboard ordered supersolid and of the supersolid below a critical value of the detuning Δ_c (determined in the frozen limit). The similarity of the results for the two geometries can be attributed to the low density of atoms and the large wavelength of the observed ordered structures when compared to the lattice spacing. We have also expanded the previous research by analyzing the properties of supersolid phases in more detail. We have observed that they can be divided into two general classes distinguished by the spatial modulation of condensate fraction and by the total fraction of excited-state bosons. Comparison of the B-DMFT and static mean-field methods shows an overall good agreement between the two approaches. The differences are limited to small regions of the phase diagram and small phase-boundary shifts.

Furthermore, we have studied the model on a finite-size lattice with Gaussian profile of the Rabi term, where we have chosen experimentally convenient parameters. We have found a supersolid phase with a low fraction of excited atoms and a visible spatial modulation of the density. While this does not solve all of the issues that render the experiment challenging, we believe this to be the most promising approach for experimental realization of supersolid phases with Rydberg atoms.

ACKNOWLEDGMENTS

Support by the Deutsche Forschungsgemeinschaft via DFG SPP 1929 GiRyd and the high-performance computing center LOEWE-CSC is gratefully acknowledged. The authors also acknowledge useful discussions with C. Groß, S. Hollerith, W. Li, Y. Li, S. Whitlock, and J. Zeiher.

APPENDIX A: SCALING OF N_{uc} CLOSE TO Δ_c IN THE FROZEN LIMIT

Below we give a simplified argumentation for the dependence of the size of the unit cell N_{uc} on the detuning close to the critical detuning strength Δ_c in the frozen limit $J = 0$.

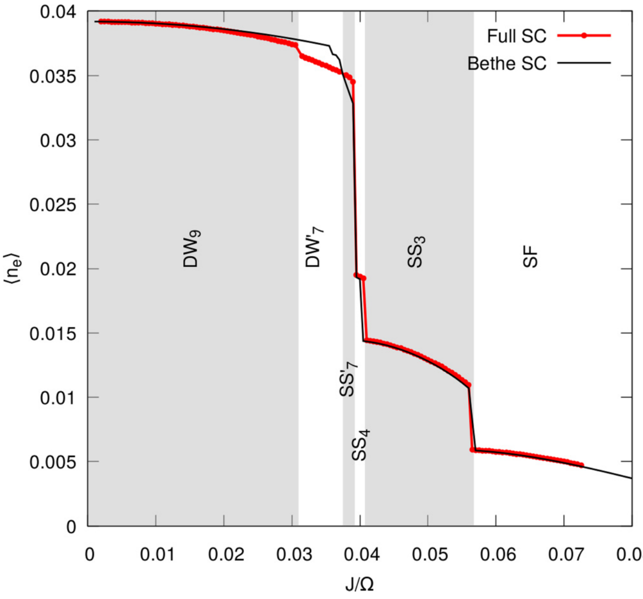

FIG. 7. Average occupation of the excited-state bosons $\langle \hat{n}_e \rangle$ as a function of hopping amplitude for $\Delta = 0$. Other parameters are the same as in Fig. 2. Red line with points represents results obtained with full B-DMFT self-consistency conditions. Black line represents results obtained with simplified self-consistency condition given by (10). Gray shading represents ranges of different phases labeled in the graph as determined by the full self-consistency.

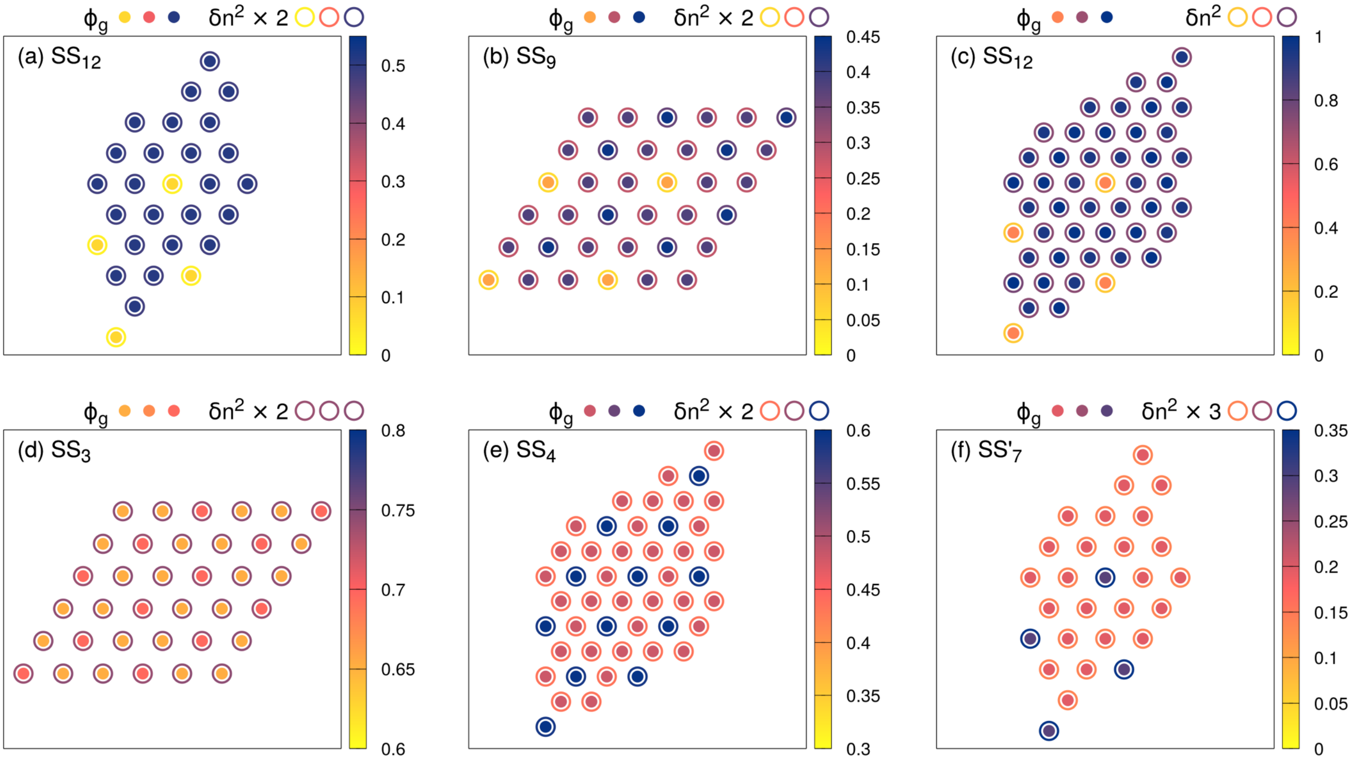

FIG. 8. Local condensate order parameter of ground-state bosons $\phi_{i,g} = \langle \hat{a}_i \rangle$ (filled circles) and local number fluctuations $\delta n_i^2 = \langle \hat{n}_i^2 \rangle - \langle \hat{n}_i \rangle^2$ (empty circles) for different phases observed in Fig. 2 at (a) $\Delta = 2.45,\ J = 0.053$; (b) $\Delta = 1,\ J = 0.046$; (c) $\Delta = 1,\ J = 0.06$; (d) $\Delta = 0,\ J = 0.045$; (e) $\Delta = 0,\ J = 0.04$; and (f) $\Delta = 0,\ J = 0.038$. Here $\hat{n}_i = \hat{n}_{g,i} + \hat{n}_{e,i}$. Each graph represents sites within a quadrupled unit cell in the same way as in Fig. 3. Note the ranges used for the SS_3 and SS_4 phases, and the rescaling of the magnitude of fluctuations used for better visibility.

We assume the system is d dimensional. We first consider the energy gain due to adding a single particle into an empty system. In such cases the only relevant energy scales in the Hamiltonian (1) are the chemical potential μ, the detuning Δ, and the Rabi frequency Ω. In order to have a finite value of Δ_c, which marks the transition of the system to vacuum, we set $\mu < 0$. Finding the single-particle eigenstates in such a case is simple and their energies are given by

$$e_\pm = -\mu - \frac{\Delta \pm \sqrt{\Delta^2 + \Omega^2}}{2}. \tag{A1}$$

The low-energy state is given by e_+, and when $e_+ < 0$ it is energetically favorable to put the particles in the system. Thus the condition $e_+ = 0$ determines the critical value of detuning Δ_c (e.g., in case of $\Omega = 1$ and $\mu = -0.25$ we get $\Delta_c = -0.75$, cf. Sec. III A). Note that this argumentation can be extended beyond the frozen limit of $J = 0$. By taking a completely delocalized single-particle state of the ground-state bosons, giving $-zJ$ contribution to the energy, one can obtain critical value of the hopping amplitude J_c as a function of the chemical potential, the detuning, and the Rabi frequency, yielding (7). We further consider the energy gain per particle in the vicinity of Δ_c, with $\Delta = \Delta_c + \delta$ and $0 < \delta \ll 1$. Expanding (A1) up to first order in δ we get

$$e_+ \approx -\frac{1}{2}\left(1 + \frac{\Delta_c}{\sqrt{\Delta_c^2 + \Omega^2}}\right)\delta. \tag{A2}$$

Therefore, energy gain per particle due to adding particles in the system is proportional to $\delta = (\Delta - \Delta_c)$.

However, upon adding particles into the system we increase the potential energy due to the van der Waals interaction. We therefore need to estimate the energy cost due to having a certain density of particles in the system. We assume that the particles form a uniform Wigner crystal with certain density $\rho \sim 1/N_{uc}$. In such cases the average distance between particles is given by $r_c \sim \rho^{-1/d}$. The energy per particle due to the van der Waals interaction can be estimated by the integral

$$e_{vdW} \sim \rho \int_{r_c}^{\infty} \frac{r^{d-1}}{r^6} \mathrm{d}r = \rho \frac{r_c^{d-6}}{6-d} \sim \rho^{6/d}. \tag{A3}$$

If we now require the energy cost of interaction to be compensated by the energy gain due to the Rabi frequency we obtain $(\Delta - \Delta_c) \sim \rho^{6/d} \sim N_{uc}^{-6/d}$, which for $d = 2$ gives $N_{uc} \sim (\Delta - \Delta_c)^{-1/3}$, cf. Fig. 1.

APPENDIX B: SUPPLEMENTARY RESULTS

1. Self-consistency test

In order to determine the accuracy of our assumption regarding the self-consistency condition (10) described in Sec. II B, we have implemented the full self-consistency condition and performed calculations for a limited range of parameters. We have chosen to set the detuning to $\Delta = 0$ and vary the hopping amplitude J, as this gives a cross section of the most interesting part of the phase diagram shown in Fig. 2. We compare the average occupation of the excited-state bosons as a function of J. The result is shown in Fig. 7.

One can see that for the majority of values of the hopping amplitude J the two self-consistency equations yield quantitatively comparable results. The major difference appears in the region of $J \in [0.031, 0.03925]$. In the simplified self-consistency the extent of the DW_7' phase is much smaller while the extent of the SS_7' phase is slightly larger. In the latter phase the simplified approach also yields a larger rate of change of the average occupation of excited-state bosons with increasing J. We note that while the extent of these phases is affected, the general features of the phase diagram remain unaffected. We do not observe significant differences, e.g., the appearance of new types of phases. Tests for other values of Δ, not shown here, confirmed this conclusion.

2. Condensate order parameter and local fluctuations

In Fig. 8 we present additional results showing local condensate fraction $\phi_{i,g} = \langle \hat{a}_i \rangle$ and local fluctuations of site occupation $\delta n_i^2 = \langle \hat{n}_i^2 \rangle - \langle \hat{n}_i \rangle^2$, for different sites i. In the phases SS_7, SS_9, and SS_{12} we observe that both the condensate order parameter and local fluctuations are significantly suppressed at the sites occupied by the excited-state bosons. This is consistent with our interpretation that in these phases we observe frozen bosons on selected sites with nonvanishing excited-state fraction and condensed bosons in the intermediate sites, which are responsible for the superflow. A qualitatively different behavior is observed for the SS_3, SS_4, and SS_7' phases. There the condensate fraction and local fluctuations are actually larger at the sites with a significant excited-state bosons fraction. This property is reminiscent of the bubble supersolids observed in Refs. [66,67], although here we work in the significantly different regime of small detuning. We note that the spatial modulation of the two observables considered here is much smaller in the SS_3 and SS_4 phase than in the SS_7' phase.

---

[1] O. Penrose and L. Onsager, Bose-Einstein condensation and liquid helium, Phys. Rev. **104**, 576 (1956).

[2] A. F. Andreev and I. M. Lifshitz, Quantum theory of defects in crystals, Zh. Eksp. Teor. Fiz. **56**, 2057 (1969) [JETP **29**, 1107 (1969)].

[3] G. V. Chester, Speculations on Bose-Einstein condensation and quantum crystals, Phys. Rev. A **2**, 256 (1970).

[4] A. J. Leggett, Can a Solid Be "Superfluid"? Phys. Rev. Lett. **25**, 1543 (1970).

[5] J. Klinder, H. Keßler, M. R. Bakhtiari, M. Thorwart, and A. Hemmerich, Observation of a Superradiant Mott Insulator in the Dicke-Hubbard Model, Phys. Rev. Lett. **115**, 230403 (2015).

[6] R. Landig, L. Hruby, N. Dogra, M. Landini, R. Mottl, T. Donner, and T. Esslinger, Quantum phases from competing short- and long-range interactions in an optical lattice, Nature (London) **532**, 476 (2016).

[7] J. Léonard, A. Morales, P. Zupancic, T. Esslinger, and T. Donner, Supersolid formation in a quantum gas breaking a continuous translational symmetry, Nature (London) **543**, 87 (2017).

[8] J. Léonard, A. Morales, P. Zupancic, T. Donner, and T. Esslinger, Monitoring and manipulating Higgs and Goldstone modes in a supersolid quantum gas, Science **358**, 1415 (2017).

[9] T. Lahaye, C. Menotti, L. Santos, M. Lewenstein, and T. Pfau, The physics of dipolar bosonic quantum gases, Rep. Prog. Phys. **72**, 126401 (2009).

[10] W Hofstetter and T Qin, Quantum simulation of strongly correlated condensed matter systems, J. Phys. B **51**, 082001 (2018).

[11] L. Tanzi, E. Lucioni, F. Famà, J. Catani, A. Fioretti, C. Gabbanini, R. N. Bisset, L. Santos, and G. Modugno, Observation of a Dipolar Quantum Gas with Metastable Supersolid Properties, Phys. Rev. Lett. **122**, 130405 (2019).

[12] F. Böttcher, J.-N. Schmidt, M. Wenzel, J. Hertkorn, M. Guo, T. Langen, and T. Pfau, Transient Supersolid Properties in an Array of Dipolar Quantum Droplets, Phys. Rev. X **9**, 011051 (2019).

[13] G. G. Batrouni and R. T. Scalettar, Phase Separation in Supersolids, Phys. Rev. Lett. **84**, 1599 (2000).

[14] K. Góral, L. Santos, and M. Lewenstein, Quantum Phases of Dipolar Bosons in Optical Lattices, Phys. Rev. Lett. **88**, 170406 (2002).

[15] H. A. Gersch and G. C. Knollman, Quantum cell model for bosons, Phys. Rev. **129**, 959 (1963).

[16] M. P. A. Fisher, P. B. Weichman, G. Grinstein, and D. S. Fisher, Boson localization and the superfluid-insulator transition, Phys. Rev. B **40**, 546 (1989).

[17] S. Wessel and M. Troyer, Supersolid Hard-Core Bosons on the Triangular Lattice, Phys. Rev. Lett. **95**, 127205 (2005).

[18] D. Heidarian and K. Damle, Persistent Supersolid Phase of Hard-Core Bosons on the Triangular Lattice, Phys. Rev. Lett. **95**, 127206 (2005).

[19] R. G. Melko, A. Paramekanti, A. A. Burkov, A. Vishwanath, D. N. Sheng, and L. Balents, Supersolid Order from Disorder: Hard-Core Bosons on the Triangular Lattice, Phys. Rev. Lett. **95**, 127207 (2005).

[20] M. Boninsegni and N. Prokof'ev, Supersolid Phase of Hard-Core Bosons on a Triangular Lattice, Phys. Rev. Lett. **95**, 237204 (2005).

[21] A. van Otterlo, K.-H. Wagenblast, R. Baltin, C. Bruder, R. Fazio, and G. Schön, Quantum phase transitions of interacting bosons and the supersolid phase, Phys. Rev. B **52**, 16176 (1995).

[22] T. Ohgoe, T. Suzuki, and N. Kawashima, Novel mechanism of supersolid of ultracold polar molecules in optical lattices, J. Phys. Soc. Jpn. **80**, 113001 (2011).

[23] S. Yi, T. Li, and C. P. Sun, Novel Quantum Phases of Dipolar Bose Gases in Optical Lattices, Phys. Rev. Lett. **98**, 260405 (2007).

[24] B. Capogrosso-Sansone, C. Trefzger, M. Lewenstein, P. Zoller, and G. Pupillo, Quantum Phases of Cold Polar Molecules in 2D Optical Lattices, Phys. Rev. Lett. **104**, 125301 (2010).

[25] J. Schachenmayer, I. Lesanovsky, A. Micheli, and A. J. Daley, Dynamical crystal creation with polar molecules or Rydberg atoms in optical lattices, New J. Phys. **12**, 103044 (2010).

[26] Z. Lan, J. Minář, E. Levi, W. Li, and I. Lesanovsky, Emergent Devil's Staircase without Particle-Hole Symmetry in Rydberg Quantum Gases with Competing Attractive and Repulsive Interactions, Phys. Rev. Lett. **115**, 203001 (2015).

[27] P. Bak and R. Bruinsma, One-Dimensional Ising Model and the Complete Devil's Staircase, Phys. Rev. Lett. **49**, 249 (1982).

[28] A. Lauer, D. Muth, and M. Fleischhauer, Transport-induced melting of crystals of Rydberg dressed atoms in a one-dimensional lattice, New J. Phys. **14**, 095009 (2012).

[29] L. Rademaker, Y. Pramudya, J. Zaanen, and V. Dobrosavljević, Influence of long-range interactions on charge ordering phenomena on a square lattice, Phys. Rev. E **88**, 032121 (2013).

[30] T. F. Gallagher, Rydberg atoms, Rep. Prog. Phys. **51**, 143 (1988).

[31] K. Singer, M. Reetz-Lamour, T. Amthor, S. Folling, M. Tscherneck, and M. Weidemüller, Spectroscopy of an ultracold Rydberg gas and signatures of Rydberg-Rydberg interactions, J. Phys. B **38**, S321 (2005).

[32] M. Saffman, T. G. Walker, and K. Mølmer, Quantum information with Rydberg atoms, Rev. Mod. Phys. **82**, 2313 (2010).

[33] H. Weimer, R. Löw, T. Pfau, and H. P. Büchler, Quantum Critical Behavior in Strongly Interacting Rydberg Gases, Phys. Rev. Lett. **101**, 250601 (2008).

[34] V. Bendkowsky, B. Butscher, J. Nipper, J. P. Shaffer, R. Löw, and T. Pfau, Observation of ultralong-range Rydberg molecules, Nature (London) **458**, 1005 (2009).

[35] T. Niederprüm, O. Thomas, T. Manthey, T. M. Weber, and H. Ott, Giant Cross Section for Molecular Ion Formation in Ultracold Rydberg Gases, Phys. Rev. Lett. **115**, 013003 (2015).

[36] T. M. Weber, M. Höning, T. Niederprüm, T. Manthey, O. Thomas, V. Guarrera, M. Fleischhauer, G. Barontini, and H. Ott, Mesoscopic Rydberg-blockaded ensembles in the superatom regime and beyond, Nat. Phys. **11**, 157 (2015).

[37] J. Zeiher, P. Schauß, S. Hild, T. Macrì, I. Bloch, and C. Gross, Microscopic Characterization of Scalable Coherent Rydberg Superatoms, Phys. Rev. X **5**, 031015 (2015).

[38] A. Browaeys, D. Barredo, and T. Lahaye, Experimental investigations of dipole-dipole interactions between a few Rydberg atoms, J. Phys. B **49**, 152001 (2016).

[39] P. Schauß, M. Cheneau, M. Endres, T. Fukuhara, S. Hild, A. Omran, T. Pohl, C. Gross, S. Kuhr, and I. Bloch, Observation of spatially ordered structures in a two-dimensional Rydberg gas, Nature (London) **491**, 87 (2012).

[40] P. Schauß, J. Zeiher, T. Fukuhara, S. Hild, M. Cheneau, T. Macrì, T. Pohl, I. Bloch, and C. Gross, Crystallization in Ising quantum magnets, Science **347**, 1455 (2015).

[41] J. Zeiher, R. Van Bijnen, P. Schauß, S. Hild, J. Choi, T. Pohl, I. Bloch, and C. Gross, Many-body interferometry of a Rydberg-dressed spin lattice, Nat. Phys. **12**, 1095 (2016).

[42] J. Zeiher, J. Y. Choi, A. Rubio-Abadal, T. Pohl, R. van Bijnen, I. Bloch, and C. Gross, Coherent Many-Body Spin Dynamics in a Long-Range Interacting Ising Chain, Phys. Rev. X **7**, 041063 (2017).

[43] P. Schauss, Quantum simulation of transverse Ising models with Rydberg atoms, Quantum Sci. Technol. **3**, 023001 (2018).

[44] T. Pohl, E. Demler, and M. D. Lukin, Dynamical Crystallization in the Dipole Blockade of Ultracold Atoms, Phys. Rev. Lett. **104**, 043002 (2010).

[45] B. Vermersch, M. Punk, A. W. Glaetzle, C. Gross, and P. Zoller, Dynamical preparation of laser-excited anisotropic Rydberg crystals in 2D optical lattices, New J. Phys. **17**, 013008 (2015).

[46] K. Saha, S. Sinha, and K. Sengupta, Phases and collective modes of Rydberg atoms in an optical lattice, Phys. Rev. A **89**, 023618 (2014).

[47] A. Geißler, I. Vasić, and W. Hofstetter, Condensation versus long-range interaction: Competing quantum phases in bosonic optical lattice systems at near-resonant Rydberg dressing, Phys. Rev. A **95**, 063608 (2017).

[48] Y. Li, A. Geißler, W. Hofstetter, and W. Li, Supersolidity of lattice bosons immersed in strongly correlated Rydberg dressed atoms, Phys. Rev. A **97**, 023619 (2018).

[49] A. Geißler, U. Bissbort, and W. Hofstetter, Quasiparticle spectra of supersolid lattice gases at near-resonant Rydberg dressing, Phys. Rev. A **98**, 063635 (2018).

[50] H. Weimer, Variational Principle for Steady States of Dissipative Quantum Many-Body Systems, Phys. Rev. Lett. **114**, 040402 (2015).

[51] S. Ray, S. Sinha, and K. Sengupta, Phases, collective modes, and nonequilibrium dynamics of dissipative Rydberg atoms, Phys. Rev. A **93**, 033627 (2016).

[52] M. Barbier, A. Geißler, and W. Hofstetter, Decay-dephasing-induced steady states in bosonic Rydberg-excited quantum gases in an optical lattice, Phys. Rev. A **99**, 033602 (2019).

[53] C. Becker, P. Soltan-Panahi, J. Kronjäger, S. Dörscher, K. Bongs, and K. Sengstock, Ultracold quantum gases in triangular optical lattices, New J. Phys. **12**, 065025 (2010).

[54] T. Manthey, T. Niederprüm, O. Thomas, and H. Ott, Dynamically probing ultracold lattice gases via Rydberg molecules, New J. Phys. **17**, 103024 (2015).

[55] B. Misra and E. C. G. Sudarshan, The Zeno's paradox in quantum theory, J. Math. Phys. **18**, 756 (1977).

[56] J. J. García-Ripoll, S. Dürr, N. Syassen, D. M. Bauer, M. Lettner, G. Rempe, and J. I. Cirac, Dissipation-induced hard-core boson gas in an optical lattice, New J. Phys. **11**, 013053 (2009).

[57] I. Vidanović, D. Cocks, and W. Hofstetter, Dissipation through localized loss in bosonic systems with long-range interactions, Phys. Rev. A **89**, 053614 (2014).

[58] K. Byczuk and D. Vollhardt, Correlated bosons on a lattice: Dynamical mean-field theory for Bose-Einstein condensed and normal phases, Phys. Rev. B **77**, 235106 (2008).

[59] J. W. Negele and H. Orland, *Quantum Many-Particle Systems* (Westview Press, Boulder, CO, 1998).

[60] S. J. Lee, B. Kim, and J. Lee, Infinite ground state degeneracy and glassy dynamics in the frustrated xy model and lattice Coulomb gas with f=16, Phys. A (Amsterdam, Neth.) **315**, 314 (2002), .

[61] A. Hubener, M. Snoek, and W. Hofstetter, Magnetic phases of two-component ultracold bosons in an optical lattice, Phys. Rev. B **80**, 245109 (2009).

[62] W.-J. Hu and N.-H. Tong, Dynamical mean-field theory for the Bose-Hubbard model, Phys. Rev. B **80**, 245110 (2009).

[63] A. Georges, G. Kotliar, W. Krauth, and M. J. Rozenberg, Dynamical mean-field theory of strongly correlated fermion

systems and the limit of infinite dimensions, Rev. Mod. Phys. **68**, 13 (1996).

[64] H. U. R. Strand, M. Eckstein, and P. Werner, Nonequilibrium Dynamical Mean-Field Theory for Bosonic Lattice Models, Phys. Rev. X **5**, 011038 (2015).

[65] The condensate of the excited-state bosons is small throughout the system, with total fraction an order of magnitude smaller than that of the ground-state bosons. Interestingly, even close to the DW_9 phase it shows ordering later observed in SS_3 supersolid.

[66] N. Henkel, F. Cinti, P. Jain, G. Pupillo, and T. Pohl, Supersolid Vortex Crystals in Rydberg-Dressed Bose-Einstein Condensates, Phys. Rev. Lett. **108**, 265301 (2012).

[67] F. Cinti, T. Macrì, W. Lechner, G. Pupillo, and T. Pohl, Defect-induced supersolidity with soft-core bosons, Nat. Commun. **5**, 3235 (2014).

[68] S. Prestipino, A. Sergi, and E. Bruno, Freezing of soft-core bosons at zero temperature: A variational theory, Phys. Rev. B **98**, 104104 (2018).

[69] S. Prestipino, A. Sergi, and E. Bruno, Clusterization of weakly-interacting bosons in one dimension: An analytic study at zero temperature, J. Phys. A: Math. Theor. **52**, 015002 (2018).

[70] I. I. Beterov, I. I. Ryabtsev, D. B. Tretyakov, and V. M. Entin, Quasiclassical calculations of blackbody-radiation-induced depopulation rates and effective lifetimes of Rydberg ns, np, and nd alkali-metal atoms with $n \leqslant 80$, Phys. Rev. A **79**, 052504 (2009).

[71] T. Boulier, E. Magnan, C. Bracamontes, J. Maslek, E. A. Goldschmidt, J. T. Young, A. V. Gorshkov, S. L. Rolston, and J. V. Porto, Spontaneous avalanche dephasing in large Rydberg ensembles, Phys. Rev. A **96**, 053409 (2017).